Solar Energy 288 (2025) 113327

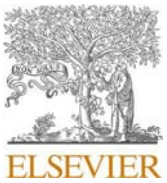

Contents lists available at ScienceDirect

Solar Energy

journal homepage: www.elsevier.com/locate/solener

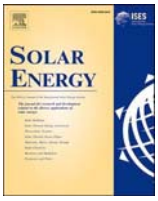

Growth manipulation in electrodeposition of compact and mesoporous electron transport layers for enhanced efficiency and stability in carbon-based perovskite solar cells

Tecush Mohammadi [a], Dimitris A. Chalkias [b], Nigel Van de Velde [a], Andrej Race [a], Elias Stathatos [b], Boštjan Genorio [c], Blaž Likozar [a], Ivan Jerman [a,*]

[a] National Institute of Chemistry, Hajdrihova 19, 1000 Ljubljana, Slovenia
[b] Department of Electrical and Computer Engineering, University of the Peloponnese, GR26334 Patras, Greece
[c] University of Ljubljana, Faculty of Chemistry and Chemical Technology, Večna pot 113, 1000 Ljubljana, Slovenia

ARTICLE INFO

Keywords:
Perovskite solar cell
Electron transport layer
TiO_2 electrodeposition
Compact layer
Mesoporous layer
Photovoltaic performance

ABSTRACT

Electrodeposition is a low-cost and mature industrial technique for large-scale perovskite solar cells (PSCs) manufacturing. The present work provides new insights into developing compact and mesoporous electron transport layers for PSCs via the electrodeposition technique in one pot. By the precise control of current density and deposition duration during the process, both the compact blocking layer and mesoporous layer can be stepwise developed, with optimized structural, morphological and optoelectrical characteristics for solar cells application. Herein, TiO_2 electrodeposited thin films are developed, with low defect density, high crystallinity and beneficial morphology for their subsequent application as substrates for perovskite heterogeneous nucleation. In this direction, the scalable electrodeposited PSCs developed under the optimized manufacturing protocol demonstrated power conversion efficiency (PCE) up to 10.83 %, significantly surpassing the 6.85 % record of the spin-coated devices. The increased light harvesting efficiency, enhanced absorbed-photon-to-electron quantum efficiency and low charge recombination losses in the electrodeposited solar cells were identified as determent factors for this PCE enhancement. The stability of the unencapsulated devices under ISOS-D-1 protocol conditions was also found increased, with their T_{70} exceeding 1000 h. This study highlights a scalable approach for the development of highly efficient and stable perovskite photovoltaics.

1. Introduction

With rising global energy demand, the need for sustainable and efficient energy harvesting is critical [1,2]. Traditional silicon photovoltaic (PV) cells face challenges such as high cost, limited material availability and low power conversion efficiency (*PCE*) [3,4]. Recently, perovskite solar cells (PSCs) have emerged as a promising alternative, offering high efficiency and low production costs. Perovskite materials like $CH_3NH_3PbI_3$ exhibit superior optoelectronic properties, including tunable bandgaps and high absorption coefficients, making PSCs strong candidates for next-generation solar energy solutions, potentially surpassing silicon PVs [5,6]. However, challenges related to stability, scalability and material interface engineering remain for commercial viability [5,7]. Among PSC architectures, n-i-p structured carbon-based PSCs (Fig. 1a) are gaining attention due to their lower cost, enhanced stability and scalability [8]. The carbon electrode serves as both the hole transport layer and back contact, making this design cost-effective and moisture-resistant [8,9].

The electron transport layer (ETL) and its buried interface with the perovskite layer are critical for n-i-p carbon-based PSC performance [10]. The heterojunction interface between materials boosts performance by enabling efficient charge transport [11,12]. This buried interface influences charge extraction, recombination dynamics and device efficiency [13]. The extended surface area at this interface is crucial for light absorption, especially in materials with short charge-diffusion lengths. Therefore, selecting suitable materials, optimizing morphologies and refining the interface are key points for achieving high *PCE* and long-term stability [12,14,15]. Titanium dioxide (TiO_2) is a widely used ETL material due to its suitable band alignment and stability. Its conduction band minimum (CBM) at 4.1 eV, along with a

* Corresponding author.
E-mail address: ivan.jerman@ki.si (I. Jerman).

https://doi.org/10.1016/j.solener.2025.113327
Received 18 October 2024; Received in revised form 30 January 2025; Accepted 1 February 2025
Available online 5 February 2025

substantial bandgap (3.0 eV for rutile and 3.2 eV for anatase), enables efficient electron injection from the perovskite absorber while blocking holes. The slightly lower CBM of TiO_2 than that of $MAPbI_3$ (3.9 eV) ensures effective electron transfer, and its low-energy valence band maximum (VBM) enhances hole-blocking properties [16].

A high-performance ETL is typically built using a two-layer structure: a compact blocking layer (BL) and a scaffold mesoporous layer (ML) (Fig. 1a). This design ensures good TiO_2-perovskite contact, improving electron transport [17–20]. The BL prevents electron recombination and blocks electron flow from the fluorine-doped tin oxide (FTO) substrate to the hole transport layer (HTL) (Fig. 1b). The ML increases surface area for charge collection, reducing series resistance. It also enhances light scattering and absorption in the perovskite layer due to large grains size, while acting as a scaffold with uniform, size-tunable channels for better perovskite growth and morphology [16,21].

Various techniques for fabricating ETLs, such as atomic layer deposition, magnetron sputtering and thermal evaporation, are well-established but often complex and costly. Conventional methods like spin-coating or spray pyrolysis tend to produce non-uniform layers with pinholes, leading to higher recombination losses [22]. Electrodeposition, a scalable and low-temperature process, has emerged as a promising alternative for fabricating high-quality ETLs, offering precise control over thickness and morphology [23,24]. This method is easily adaptable and cost-effective, making it appealing for TiO_2 ETL fabrication [25,26]. Recent studies show that electrodeposited TiO_2 compact layers with brookite scaffolds enhance electron extraction and reduce hysteresis in PSCs [21], while improved fill factor (*FF*) and open-circuit voltage (V_{OC}) values have been reported with mesoporous TiO_2 layers [27]. Despite these advancements, optimizing electrodeposition parameters for both compact and mesoporous layers remains a challenge, and understanding their combined effect on device performance is crucial.

This work introduces a novel approach to optimize the ETL in carbon-based PSCs through a comprehensive study of electrodeposition. We examine how varying current densities and deposition times affect the characteristics of both compact and mesoporous TiO_2 layers. Our study uniquely combines the optimization of these two critical ETL components to achieve a synergistic effect, enhancing electron mobility, reducing recombination losses and improving overall device efficiency. The results mark significant progress in developing more efficient and stable PSCs by focusing on electrodeposited ETLs, addressing both performance and scalability challenges in ETL fabrication, and contributing to advancements in PV technology.

2. Materials and methods

2.1. Chemicals

FTO glass (Pilkington), zinc dust (≥98 %, Acros), hydrochloric acid (≥37 %, Fluka) and acetone (Euriso-top) were purchased for patterning the cell substrate.

The electrolyte for electrodeposition of the ETL was prepared using titanium (III) chloride (10–15 % in HCl, Sigma Aldrich) and ethylenediaminetetraacetic acid (EDTA (2Na), Fluka). Sodium carbonate (99.9 %, Sigma Aldrich) and sodium hydroxide (98 %, Fluka) were used to adjust the pH and for the pre-treatment of FTO Glass, respectively. For spin-coated TiO_2, a mixture of titanium(diisopropoxide) bis(2,4-pentanedionate) (75 wt% in Isopropanol, Alfa Aesar), and Isopropanol (99.5 %, Sigma Aldrich) were used.

To prepare the perovskite precursor solution, lead (II) iodide (ultra-dry, 99.99 %, Tokyo Chemical Industry) and methyl ammonium iodide (MAI, 99.99 %, Great Cell Solar Materials) were dissolved in a 4:1 mixture of N,N-dimethylformamide (DMF, 99.9 %, Sigma Aldrich) and dimethyl sulfoxide (DMSO, 99.8 %, Sigma Aldrich). Chlorobenzene (≥99 %, Merck) was used as an anti-solvent, and a layer of conductive carbon paste (Dyenamo) was applied on top of the perovskite layer.

For the electrochemical measurements, a solution containing sodium sulfite (≥98 %, Sigma Aldrich), sodium sulfate (≥99.0 %, Merck),

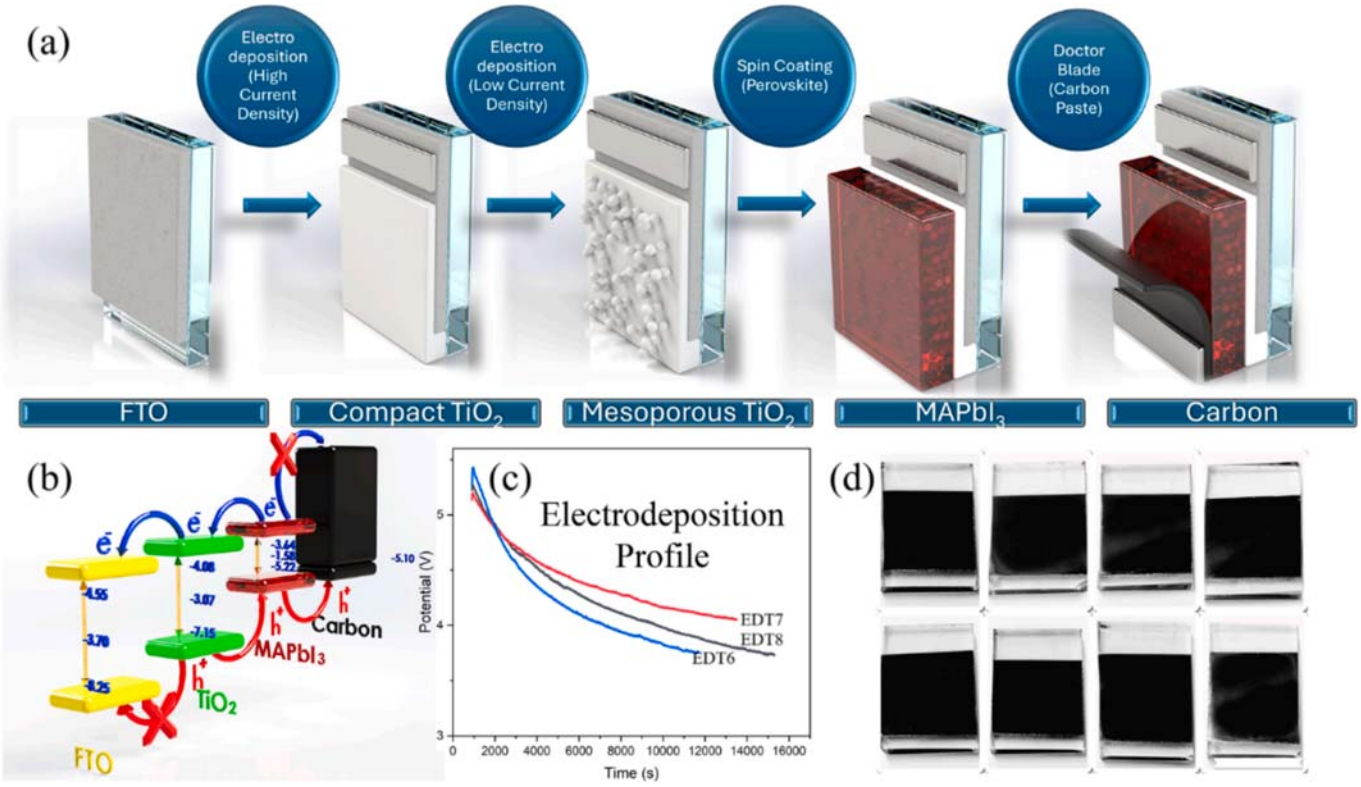

Fig. 1. (a) Schematic of TiO_2 electrodeposition and spin-coating of the perovskite layer for PSC fabrication; (b) Energy level diagram for various layers in a carbon-based PSC; (c) Potential vs. time profile during TiO_2 electrodeposition; (d) Fabricated solar cells.

potassium hexacyanoferrate (III) (99 %, Fluka), potassium hexacyanoferrate (II) trihydrate (≥99.0 %, Kemika) and potassium chloride (99 %, Sigma Aldrich) was prepared.

2.2. Preparation of electrodeposited TiO_2 (ED-TiO_2)

TiO_2 electrodeposition on FTO was carried out anodically under varying current densities, as shown in Table 1, and the samples were labeled EDT1 to EDT8. Prior to deposition, FTO glass was etched using zinc powder and concentrated HCl. The substrates were then ultrasonicated in acetone for 20 min and in deionized water for 30 min, followed by drying in air. A pre-treatment of anodic oxidation was performed in 1 M NaOH with a 2 mA cm^{-2} current density to improve film uniformity and adhesion. After rinsing in deionized water, the substrates were immediately used for electrodeposition. The electrodeposition mechanism is provided in the supporting information.

Electrodeposition was carried out in a solution of 0.25 M titanium (III) chloride and 0.018 M EDTA under a nitrogen atmosphere. The pH was adjusted to 2.5 using sodium carbonate. During deposition, the solution was stirred with a Teflon stir bar on a magnetic hot plate at room temperature. After deposition, the samples were rinsed with deionized water, dried in air and annealed at 480 °C for 1 h.

Electrochemical experiments were performed using a custom 3D-printed polypropylene cell with a three-electrode system. A saturated Ag/AgCl electrode and a platinum plate (5 × 1.5 cm^2) were used as the reference and counter electrodes, respectively.

2.3. Cell fabrication

The 1.5 M perovskite precursor solution, composed of lead (II) iodide and methyl ammonium iodide in a DMF/DMSO mixture (4:1), was prepared in a glovebox. The solution was stirred at 60 °C for 3 h until fully dissolved. The electrodeposited TiO_2 FTO substrates were cleaned by heating at 480 °C for 15 min to remove organic residues, followed by 15 min of UV-O_3 cleaning using an Ossila UV ozone cleaner. The cleaned substrates were immediately used for cell fabrication.

In a nitrogen-controlled environment with 23 % humidity, 40 μL of perovskite solution was spin-coated onto 1 cm^2 substrates at 5000 rpm for 25 s using a Laurell ws-650-23 spin coater. At 9.5 s into the spin-coating process, 260 μL of chlorobenzene was dropped onto the surface as an antisolvent at 13.5 mL min^{-1}. After spin-coating, the samples were annealed at 100 °C for 10 min on a preheated hot plate, and were placed in a glovebox for 24 h for stabilization. Carbon paste was then applied using a glass rod, with the thickness controlled by a 0.05 mm spacer. The samples were finally annealed at 80 °C for 1 h to evaporate the solvent. A control cell was fabricated using spin-coated TiO_2 as ETL.

2.4. Material characterization

The crystalline phases of the TiO_2 film and perovskite were identified via X-ray diffraction (XRD) using a Bruker D8 Advance diffractometer. Scanning was performed at 2° per minute within a 2θ range of 10° to 80°.

Since EDT7 had optimal deposition conditions, X-ray photoelectron spectroscopy (XPS) was conducted on its surface and depth using a Versaprobe 3 AD (Phi, Chanhassen, US) with a monochromatic Al-Kα1 X-ray source. Spectra were recorded with a 200 μm spot size (43.2 W, 45.0°, 224 eV pass energy), while surface mappings were captured with a 6.6 μm spot size (0.8 W, 45.0°). Data were analyzed using PHI Multipak software.

The surface and cross-sectional morphology were characterized using field emission scanning electron microscopy (FE-SEM) on a FEI Inspect F50 microscope. Top-view images were taken with a 1.5 kV acceleration voltage and 20,000× magnification, while cross-sectional images of freshly cleaved samples were captured at 5 kV and 40,000× magnification.

AFM surface profiling was conducted with a WiTec Alpha 300 RA confocal microscope (WiTec, Ulm, Germany) in AC tapping mode using reflex-coated AFM sensors (2.8 N/m, 75 kHz). Scans had a resolution of 512 × 512 data points with a line scan speed of 1 s/l. First-order line flattening corrected for tilt before image extraction and statistics. Both roughness and height features (2D profile images) and basic material characteristics (phase images) were obtained.

The contact angle of EDT1-EDT8 with water and the perovskite precursor was measured using a Theta T200 contact angle analyzer.

Absorbance and reflectance spectra in the UV–VIS range (300–800 nm) were measured using a Jasco V-770 spectrophotometer with a 60 mm integrating sphere and a PbS detector (ISN-923), at a 5 nm interval.

2.5. Electrochemical characterization, quantum efficiency determination and J-V measurements

All electrochemical measurements were performed using a computer-controlled potentiostat–galvanostat (Autolab PGSTAT302N with a frequency response analyzer (FRA)) in an aqueous electrolyte containing 0.5 mM potassium hexacyanoferrate (II) trihydrate, 0.5 mM potassium hexacyanoferrate (III), and 0.5 M potassium chloride for enhanced ionic conductivity. A three-electrode system was used, with electrodeposited TiO_2 on FTO glass (FTO/TiO_2), Ag/AgCl and a 1 cm^2 platinum electrode as the working, reference and counter electrodes, respectively. The blocking effect of the FTO/TiO_2 BL was investigated by cyclic voltammetry (CV) at a 50 mV s^{-1} scan rate. The scan range was −0.5 V to +1.0 V, starting at 0.0 V for 2 scans, with the second scan used for reporting. Linear sweep voltammetry (LSV) of FTO/TiO_2 was measured in the dark and under illumination. Electrochemical impedance spectroscopy (EIS) was performed on FTO/TiO_2 samples and PSCs based on FTO/TiO_2. The scanning frequency range was 100 kHz to 1 Hz, with an applied bias voltage set to the V_{OC} and an AC amplitude of 5 mV.

A solar simulator (Solar Light 16S-300) with a source meter (Keithley 2601) under 100 mW cm^{-2} AM 1.5G illumination was used for J-V measurements of the PSCs. The irradiance was calibrated using a reference monocrystalline silicon cell (Newport 71750 V) (Newport 2420). The applied bias voltage ranged from −0.1 to +1.0 V for the forward scan (FS) and +1.0 to −0.1 V for the reverse scan (RS), with a

Table 1
Electrodeposition parameters for blocking and mesoporous layers.

Sample	Compact layer (Blocking layer)			Mesoporous layer			ETL
	Current Density (μA cm^{-2})	Time (s)	Charge (C cm^{-2}) × 10^{-2}	Current Density (μA cm^{-2})	Time (s)	Charge (C cm^{-2}) × 10^{-2}	Charge (C cm^{-2}) × 10^{-2}
EDT1	5	900	0.45	2.5	2400	0.60	1.05
EDT2	10	900	0.90	2	2400	0.48	1.38
EDT3	15	900	1.35	2	2400	0.48	1.83
EDT4	25	900	2.25	2	2400	0.48	2.73
EDT5	50	900	4.50	2	2400	0.48	4.98
EDT6	25	900	2.25	2	10,800	2.16	4.41
EDT7	25	900	2.25	2	12,600	2.52	4.77
EDT8	25	900	2.25	2	14,400	2.88	5.13

pre-sweep delay of 1.00 s, a dwell time of 250 ms, and 120 sweep points. The solar cell active area was fixed with a 0.075 cm^2 black shadow mask.

The external and internal quantum efficiency of the solar cells were measured using a θMetrisis PM-QE apparatus with a xenon light source and filter monochromator (Oriel Cornerstone 260 1/4 m, Newport), controlled by PM-Monitor software. Measurements were taken from 300 nm to 800 nm, with a 5 nm interval wavelength and a 0.2 s delay time.

3. Results and discussions

3.1. Fabrication of ETL

Electrodeposition of TiO_2 onto conductive substrates, via oxidation or reduction, has seen decades of development. Unlike other techniques (spray pyrolysis, spin-coating, dip coating, etc.), electrodeposition offers precise control, adjustment and scalability. The morphology of the electrodeposited TiO_2 film is affected by factors like current density, deposition time, pH, and bath composition and temperature [24,26,27].

To study the effect of current density and deposition time on ETL properties, eight TiO_2 samples were electrodeposited on FTO glass, varying these parameters for both the blocking and mesoporous layers (Table 1). This approach systematically explores how electrodeposition conditions influence ETL characteristics and highly affect PV device performance. The parameters were selected to cover both practical and theoretical limits from similar studies [23,24,26,27], assessing their impact on ETL uniformity, thickness and charge transport, and offering insights into the relationship between deposition conditions and ETL performance.

Characterizing the structural properties of the ETL is crucial for enhancing the performance of PSC devices. The following section investigates these properties using various techniques.

3.2. Structural study

XRD measurements were conducted to characterize the phase structure of as-electrodeposited TiO_2/FTO (EDT7), spin-coated TiO_2/FTO, and EDT7/$MAPbI_3$ perovskite (Fig. 2). The peaks observed at 25.30°, 37.79°, 48.04°, 53.89°, 55.06°, 62.69°, 68.76° and 70.29° corresponding to the (0 0 1), (0 0 4), (0 2 0), (0 1 5), (1 2 1), (0 2 4), (1 1 6) and (2 2 0) planes of the TiO_2 anatase phase (ref. file no. 96-900-9087) for electrodeposited TiO_2. Furthermore, peaks at 25.30°, 37.79°, 48.04°, 53.89°, 55.06°, 62.69°, 68.76° and 75.05° corresponding to the (0 0 1), (0 0 4), (0 2 0), (0 1 5), (1 2 1), (0 2 4), (1 1 6) and (1 2 5) planes, respectively, are observed for the spin-coated TiO_2 film (ref. file no. 96-900-9087). Moreover, according to ref. code no. 96-100-0063, peaks at 26.58°, 33.87°, 37.95°, 51.77°, 61.88° and 65.96° correspond to the crystal planes of $Sn_{2.00}O_{4.00}$ for bare FTO glass, specifically referring to (1 1 0), (0 1 1), (0 2 0), (1 2 1), (1 3 0) and (0 3 1).

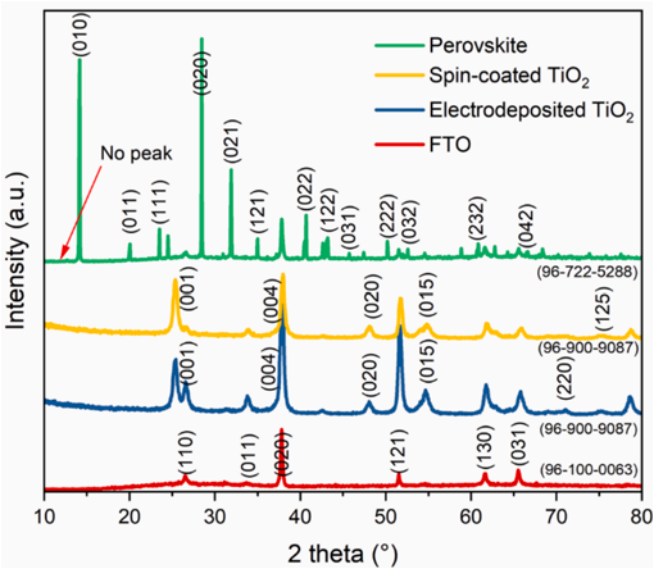

Fig. 2. XRD patterns of different materials: FTO (red), Electrodeposited TiO_2 (blue), Spin-coated TiO_2 (yellow) and Perovskite (green). The absence of peaks in perovskite at 12.5° is noted. (For interpretation of the references to colour in this figure legend, the reader is referred to the web version of this article.)

XRD pattern of $MAPbI_3$ perovskite shows the peaks at 14.11°, 20.01°, 24.56°, 28.44°, 31.88°, 35.02°, 40.65°, 50.36° and 60.85° indicating the (0 1 0), (0 1 1), (1 1 1), (0 2 0), (0 2 1), (1 2 1), (0 2 2), (2 2 2) and (2 3 2) planes of the $MAPbI_3$ perovskite phase lattice. These peaks indicate a cubic crystal system. To assess the influence of PbI_2 residuals on the morphology, crystalline structure and stability of the $MAPbI_3$ film, the pattern was examined for peaks at 12.5° associated with the PbI_2 lattice. No distinct peak was observed.

The average crystal size of the perovskite was approximately 107 nm, determined from the primary diffraction peaks (0 1 0), (0 2 0), (0 2 1) and (0 2 2) using the full width at half maximum (FWHM) and Scherrer's formula (Eq. (1)) [28]. In this formula, K is 0.9, λ is the wavelength of the X-ray radiation, and β is the line width at half-maximum height [29,30].

$$D = \frac{K\lambda}{\beta cos\theta} \quad (1)$$

XPS measurements investigated the chemical states and surface composition of the ETL at various depths, revealing surface chemistry and electronic structure. Argon etching exposed the inner layers of the films. Fig. 3 shows the XPS survey spectrum of TiO_2 samples, displaying Ti, O, Sn (from FTO) and C (likely from surface contamination). The main peaks identify core levels and Auger transitions for detected elements [31,32]. The absence of a Cl $2p_{3/2}$ peak at 199.4 eV confirms no Ti–Cl bonds, indicating complete conversion to TiO_2 [33].

Fig. 4 presents the core-level XPS spectra of electrodeposited TiO_2. In Fig. 4a, O 1s deconvolution reveals three peaks at the surface and two in the bulk. The primary peak around 526.81 eV corresponds to lattice oxygen in TiO_2 (O-Ti^{4+}). The O 1s peak at 529.71 eV is linked to surface hydroxylation from adsorbed moisture, which decreases with depth (Fig. 4b and c). The 528.21 eV peak is associated with oxygen vacancies and O-Ti^{3+} bonds, with higher intensity near the surface [31,32]. The Ti

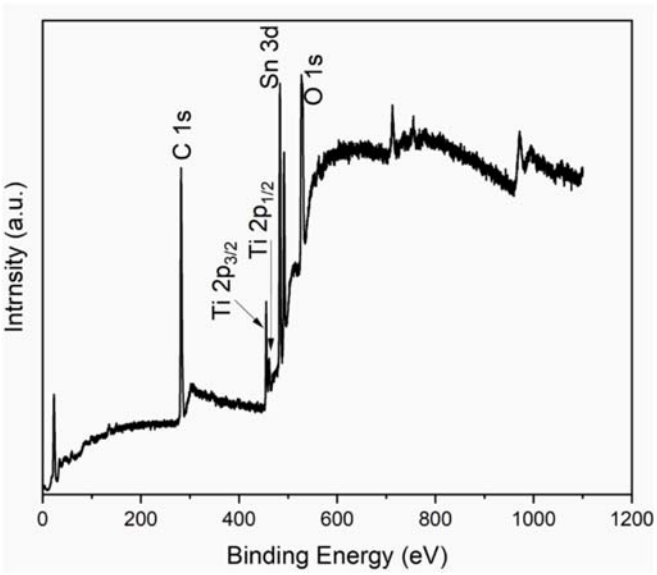

Fig. 3. XPS spectrum of electrodeposited TiO_2 film on the surface of FTO.

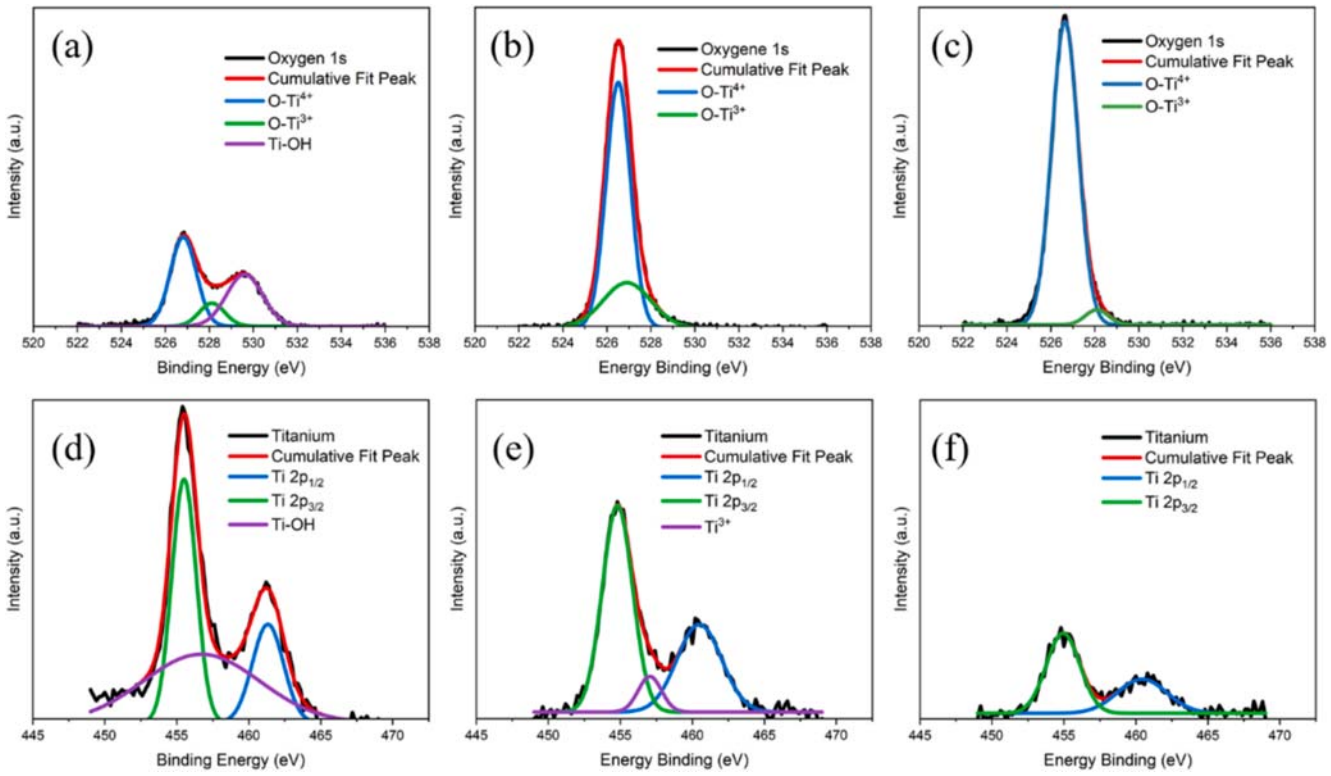

Fig. 4. High-resolution XPS Spectra of oxygen and titanium in TiO_2 film. O 1s (a) at the surface of the film, (b) after 2400 s, (c) after 4200 s of etching. Ti 2p (d) at the surface of the film, (e) after 2400 s, (f) after 4200 s of etching.

2p spectrum in Fig. 4d shows two main peaks: Ti $2p_{3/2}$ (455.38 eV) and Ti $2p_{1/2}$ (461.08 eV), characteristic of Ti^{4+} in TiO_2. The spin–orbit splitting of about 5.7 eV matches TiO_2 literature values [34]. A small peak at 457.17 eV corresponds to Ti^{3+} states attributed to defects and vacancies (Fig. 4e, f), which diminish with increasing depth [31,32].

The depth profile in Fig. 5 shows that the hydroxylated TiO_2 layer is confined to the surface and vanishes after initial etching. Titanium vacancies persist for up to 4000 s of etching, marking the boundary between mesoporous and compact layers. Peaks related to titanium species are observed up to 5400 s, suggesting this depth corresponds to the TiO_2 and FTO interface (Fig. 5a). Fig. 5b and c provide 3D plots, illustrating peak evolution during etching.

SEM and AFM were used to characterize the morphology and surface properties of the material. Fig. 6 shows SEM images of the FTO substrate after the BL (compact layer) electrodeposition, and with the compact layer followed by ML electrodeposition. Fig. 6a shows irregularly shaped bare FTO grains ranging from tens to hundreds of nanometers, contributing to surface roughness. In Fig. 6b, FTO grains are still visible, however, a thin, uniform TiO_2 film covers the surface. This compact film displays granular nanoparticles, unlike films deposited at lower current densities, which feature a less compact structure with short nanorods (Fig. 6c).

It has been shown that in $MAPbI_3$-based PSCs, TiO_2 layers with a dual structure comprising a thin, dense buffer layer (20–50 nm) and a thicker porous nanocrystalline layer (50–150 nm) (Fig. 1a) promote efficient electron transport through TiO_2 tunneling, which requires a mesoporous electron transporter (Fig. 1b) [7,21,27,35]. In the electrodeposition method, increasing the charge passed generally results in a thicker film, though a thick compact film on FTO can reduce optical transmittance and conductivity. The electrodeposited TiO_2 thickness in our approach is around 65–70 nm (Fig. 6e).

Fig. 6d shows a top-view SEM image of $MAPbI_3$ film grown using a one-step process on electrodeposited TiO_2, revealing a compact, pinhole-free surface with an average grain size of about 250 nm. Fig. 6e provides a cross-section image of the PSC device, indicating that the $MAPbI_3$ and TiO_2 layers are about 520 nm thick.

Moreover, the surface morphology of the electrodeposited TiO_2 layer on FTO glass was analyzed using AFM (Fig. 7a–c). The AFM images of the EDT7 sample show a scanned area of 5 μm × 5 μm. The three-dimensional topography in Fig. 7a reveals a uniformly rough surface with peak heights ranging from approximately −26 nm to 28 nm, indicating consistent TiO_2 deposition. The two-dimensional amplitude image and 2D topology of the film cross-section (Fig. 7b and c) highlight the granular nature of the TiO_2 film, which is vital for efficient electron transport in PSCs. Surface roughness and uniformity are critical for optimizing the interface between the ETL and the perovskite absorber, potentially enhancing device performance. The AFM analysis demonstrates the formation of a nanostructured TiO_2 layer, suitable for use in PSCs.

Further AFM analysis of the perovskite layer deposited on the electrodeposited TiO_2 shows a well-formed crystalline structure with a smooth and uniform surface (Fig. 7d). The 2D topology of the perovskite film (Fig. 7e) highlights this uniformity, which is essential for minimizing interface defects and promoting efficient charge transfer between the perovskite and the underlying ETL. The scan, covering an area of 3.5 μm × 3.5 μm, shows a peak-to-valley height of 53 nm (Fig. 7f), indicating consistent deposition that enhances overall device efficiency.

Surface morphology, including TiO_2 roughness and uniformity, can significantly influence contact angle and wettability. This relationship explains variations in contact angles and their impact on PSC performance. To assess wettability and device stability upon exposure to water (Fig. S1 in the Supporting Information) and perovskite solution (Fig. 8), contact angle measurements were performed.

The contact angles of perovskite solution on EDT1-EDT8 substrates are presented in Fig. 8a–h. The contact angle values suggest favorable wetting characteristics, indicating good compatibility of the perovskite solution with the electrodeposited layers across all samples. Variations in contact angles are attributed to differences in surface morphology and

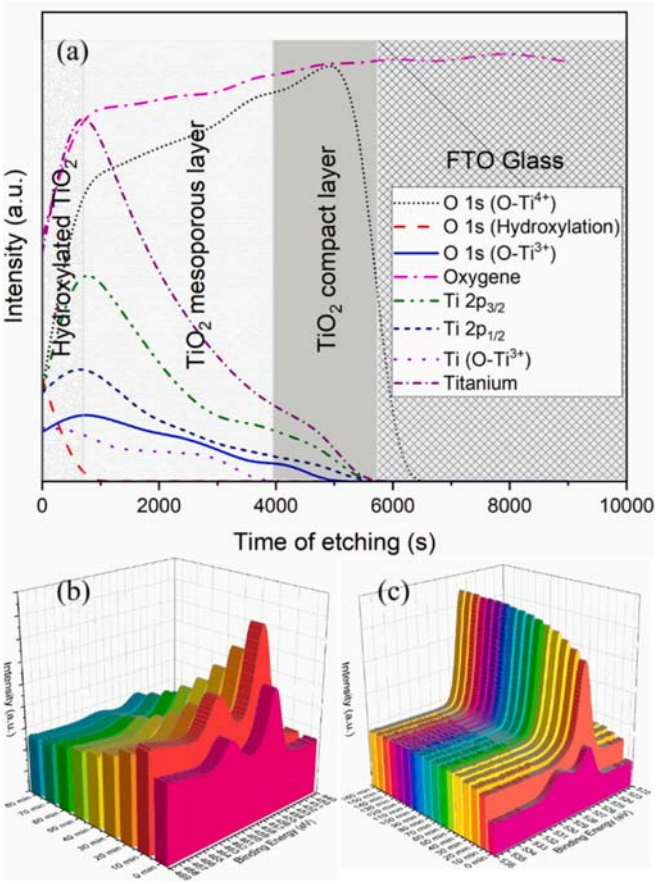

Fig. 5. (a) Depth profile composition measurements of the ETL show the relative content of Ti 2p, and O 1s as a function of ion bombardment time, which correlates to the depth from the surface into the bulk of the sample. (b) Ti 2p (c) O 1s.

roughness resulting from varying current densities and deposition times during electrodeposition. Lower contact angles, signifying higher wettability, improve the interface contact between the perovskite layer and the ETL, reducing charge accumulation at the interface and enhancing solar cell performance [36]. Conversely, higher contact angles reduce surface tension, limiting nucleation in small cavities and promoting larger grain growth, reducing recombination centers within small grain boundaries [37,38]. Balancing the contact angle is crucial; an optimal value ensures adequate wettability for efficient charge transfer while fostering the growth of larger grains, minimizing recombination losses.

The optical properties, such as the bandgap, remain consistent across all samples, as shown by the UV–vis absorbance spectra and Tauc equation-derived bandgap values (Fig. S2, Equation S1).

3.3. Electrochemical study

Electrochemical techniques like CV and LSV provide insights into semiconductor-electrolyte interface behavior. To assess the blocking effect of electrodeposited TiO_2 on FTO, CV was employed with a three-electrode setup and $Fe(CN)_6^{3-/4-}$ as the redox couple (Fig. 9). For bare FTO, a Nernstian reversible redox reaction is expected, with an ΔI_p (difference between cathodic and anodic peak currents) of about 56 mV [24]. In this study, bare FTO exhibited an ΔI_p of 70 mV, a reasonable deviation due to uncompensated resistance in the solution, wiring and contacts. This indicates that bare FTO does not impose a significant blocking effect, maintaining a reversible redox reaction.

For the TiO_2 samples, ΔI_p values varied, with EDT1-EDT8 showing 218, 288, 300, 354, 202, 334, 284 and 585 mV, respectively. This reveals a decline in the redox reaction efficiency of $Fe(CN)_6^{3-/4-}$ with increasing electrodeposition time and current density, indicating a shift to a semi-reversible process. The peak current density is given by the Randles-Sevcik Eq. (2) [21,27]:

$$I_p = 2.69 \times 10^5 \times A \times D^{1/2} \times n^{3/2} \times \nu^{1/2} \times C \quad (2)$$

When other parameters in Eq. (2) remain unchanged, the cathodic peak current density is directly proportional to the electrode area. With the surface area reduced by the BL in samples EDT1-EDT8, the cathodic peak current density (I_p) decreased. The ratio of cathodic peak current density for electrodeposited electrodes to bare FTO (I_p(BL)/I_p(FTO)) in Fig. 9 shows values of 0.23, 0.26, 0.24, 0.20, 0.32, 0.23, 0.31 and 0.16 for EDT1-EDT8, indicating robust BL coverage. The broad cathodic peaks in EDT1-EDT8 suggest a dense, compact layer, where electron transfer occurs via hopping mechanisms rather than direct contact, confirming the effective formation of the layer. The reduction in I_p highlights the impact of BL on electrochemical performance.

LSV under simulated solar light (Fig. S3) shows an increase in photocurrent density, indicating enhanced charge separation due to the TiO_2 layer, reducing recombination and improving overall activity.

In addition to LSV and CV, EIS was used to further investigate charge transfer processes and internal resistances at layer interfaces, complementing the electrochemical analysis of electrodeposited TiO_2 films and perovskite solar cells. EIS provides insights into charge transfer at the electrode/electrolyte interface, photo-induced phenomena, and current density quantification. By applying a sinusoidal voltage with varying frequency, the current response can be measured [39]. EIS assessed internal resistances and electron transport kinetics in EDT1-EDT8. Fig. 10a shows the Nyquist plot for electrodeposited TiO_2 films on FTO glass, measured in the dark. The data were analyzed using the equivalent circuit in the inset of Fig. 10a. All Nyquist plots show a small semicircle followed by a larger one, indicating charge transfer through the electrode/electrolyte interface, with a Warburg element appearing in samples with longer deposition times. A two-time constant and Warburg element equivalent circuit was used to fit the spectra. The first time constant (CPE_1 and R_p) is linked to double-layer capacitance at the TiO_2/FTO interface, while the second (CPE_2 and R_2) corresponds to interfacial processes in the compact layer and ML. The Warburg element represents diffusion-controlled processes, likely ionic or electronic diffusion in the TiO_2 film [39,40]. The charge transport resistance (R_p) at the TiO_2/electrolyte interface increased with deposition time and current density, likely due to increased TiO_2 thickness (Fig. 10a). The larger semicircle diameter grows for EDT1-EDT4 with increasing current density but decreases slightly for EDT5. EDT4 shows the largest diameter, indicating optimal current density. This diameter increases for EDT6-EDT8, with longer electrodeposition times. As current density and deposition time increased, the characteristic frequency peak shifted to lower frequencies, correlating with recombination or electron lifetimes (τ_r or τ_e) in the TiO_2 film. EDT6-EDT8 exhibit higher transport resistance and shorter electron lifetimes, reducing the charge recombination rate, suggesting improved coverage and blocking properties.

EIS spectra of PSCs typically show two arcs: a high-frequency arc related to bulk recombination and geometric capacitance, and a low-frequency arc corresponding to interfacial phenomena. EIS spectra for PSCs based on EDT1-EDT8 were recorded under open-circuit conditions with a 10 mV AC voltage over a frequency range of 100 kHz–1 Hz. The equivalent circuit proposed by Garcia-Belmonte et al. was used to fit the data (Fig. 10b) [41,42]. The circuit includes external series resistance (R_s), two constant-phase elements (CPE_1 and CPE_2), and two resistive elements (R_p and R_2) [39]. R_s values for all cells range between 14 and 16 Ω, indicating uniform internal resistance. R_p and CPE_1, in the high-frequency range, relate to charge transport resistance in the bulk perovskite and ETL. Fig. 10b shows decreasing charge transport resistance from EDT1 to EDT4, with a slight increase for EDT5, indicating

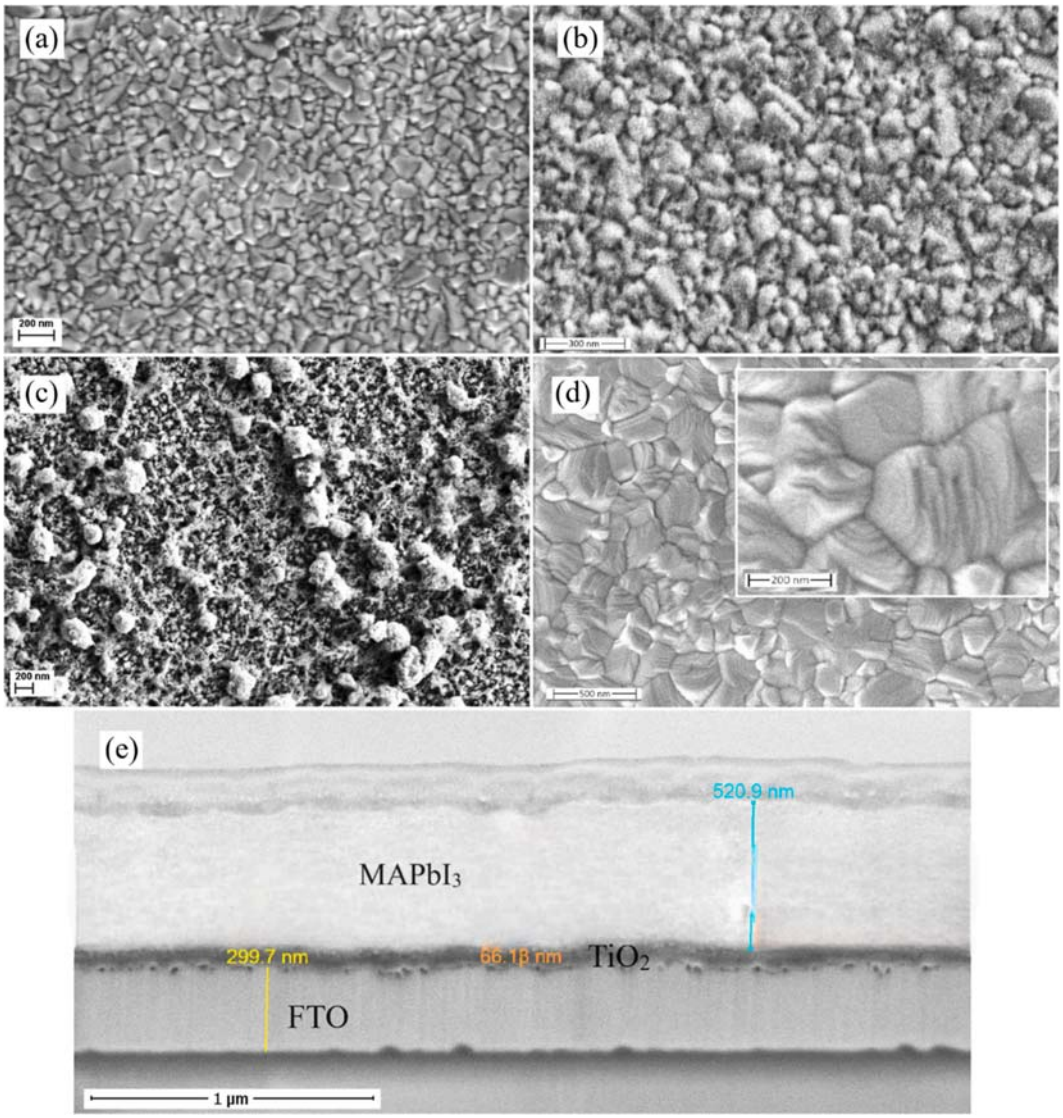

Fig. 6. SEM images of the top view and cross-section of different deposition steps for TiO_2 and perovskite films: (a) FTO substrate, (b) TiO_2 compact layer, (c) TiO_2 ML, (d) top view of the perovskite film with a magnified inset, (e) cross-sectional image of the deposited ETL and perovskite film.

improved charge flow with a more compact TiO_2 underlayer. A significant reduction in charge transport resistance with thicker mesoporous TiO_2 in EDT6-EDT8 highlights the importance of ML for higher PSC quality, although EDT8 shows a slight decline, suggesting optimal TiO_2 BL thickness (60–65 nm) for efficiency. The time constant for these cells, linked to high-frequency phenomena, ranges from 0.4 ms for EDT7 to 2.8 ms for EDT5.

The second capacitive element, CPE_2, indicates surface charge accumulation at cell interfaces, operating at lower frequencies. Low-frequency resistance, R_2, relates to accumulation resistance at interfaces and slower phenomena like trap-mediated charge recombination and ion diffusion [39]. The accumulation of electronic and ionic charges at perovskite interfaces results in significant capacitance at low frequencies. Low-frequency results and pre-perovskite EIS data highlight the role of electrodeposited TiO_2 as a BL. A dense, compact layer inhibits positive charge migration to the anode, while improved ML-perovskite contact reduces charge accumulation and recombination.

3.4. PV performance

Understanding charge dynamics and electrical properties at the interface is crucial, as they directly impact PV performance. This includes examining how electrodeposition parameters affect electron transfer efficiency, which is essential for optimizing *PCE*.

The *LHE* assesses the ability of solar cells to capture the light for its subsequent conversion into charge carriers, indicating the efficiency of light collection [43]. The *LHE* of the samples (EDT1 to EDT8) was calculated using Eq. (3):

$$LHE = (1 - R)\left(1 - 10^{-A}\right) \tag{3}$$

where A and R are the absorbance and reflectance spectra, respectively [44]. Fig. 11 shows that all samples had *LHE* values over 80 % across the visible spectrum (300–800 nm), suggesting efficient light collection.

Samples EDT6 to EDT8 showed slightly improved LHE compared to EDT1 to EDT5 due to a thicker mesoporous TiO_2 layer. This increased surface area at the interface with the perovskite allows more photons to be absorbed, enhancing light collection efficiency.

While LHE evaluates light-harvesting ability, *IPCE* and *APCE* further assess photon-to-current conversion efficiency. Fig. 12a shows IPCE spectra, where EDT6 to EDT8 exceeded 85 % across the visible spectrum (400–700 nm). IPCE reflects the fraction of absorbed photons converted into electrons, representing external quantum efficiency. The thicker TiO_2 layer in these samples improved charge generation and extraction,

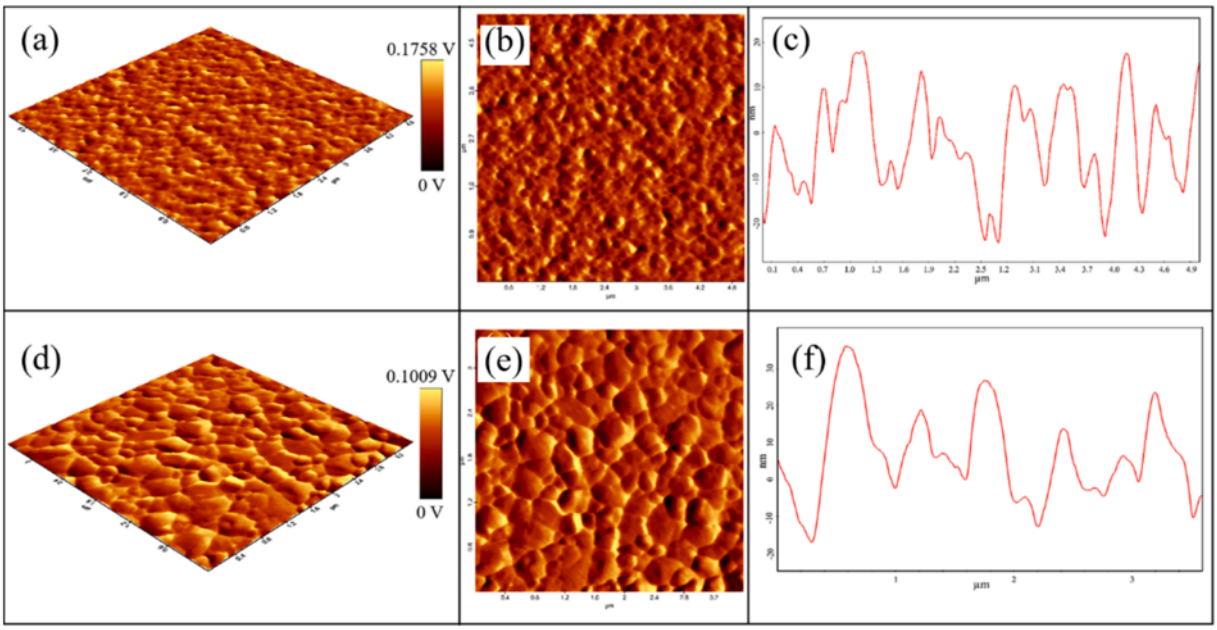

Fig. 7. AFM imaging of the surface (a and b) and 2D topology of film cross-section (c) of electrodeposited TiO_2 layer in comparison with 3D and 2D surface images (d and e) and 2D topography cross-section (f) of perovskite film.

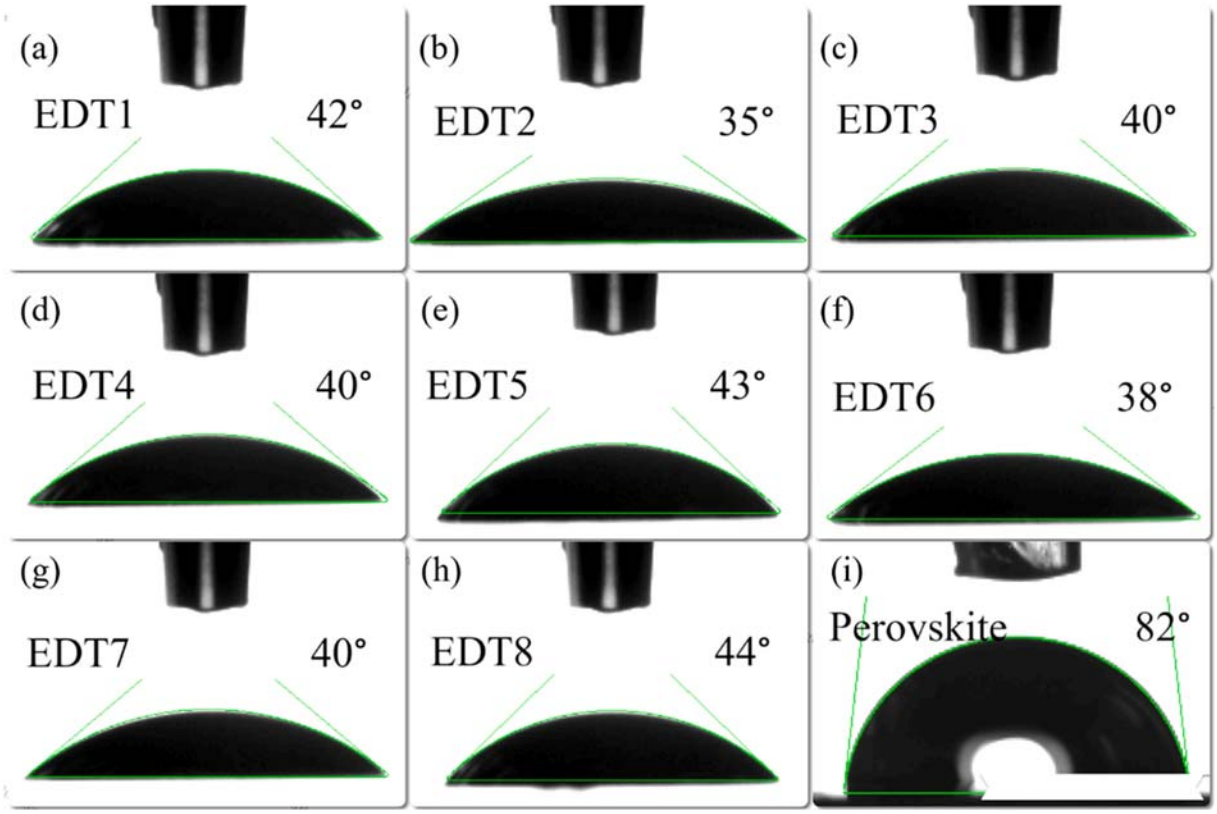

Fig. 8. (a-h) are photos of static perovskite solution contact angle results on the EDT1-EDT8 and (i) water contact angle of perovskite film, respectively.

enhancing electron transport and reducing recombination, contributing to higher short-circuit current density (J_{sc}) [45]. To assess internal efficiency, APCE was calculated using Eq. (4):

$$APCE = IPCE/LHE \tag{4}$$

As shown in Fig. 12b, *APCE* represents the fraction of absorbed photons converted into electrons, accounting for charge transport losses. Samples EDT6 to EDT8 showed nearly perfect APCE values (~100 %) in the 400–500 nm range, indicating highly efficient internal charge transport and extraction.

The relation between *IPCE* and *APCE* illustrates the interaction between external and internal efficiencies. While *IPCE* measures photon-to-electron conversion (external efficiency), *APCE* accounts for internal charge collection. Improved performance in EDT6 to EDT8

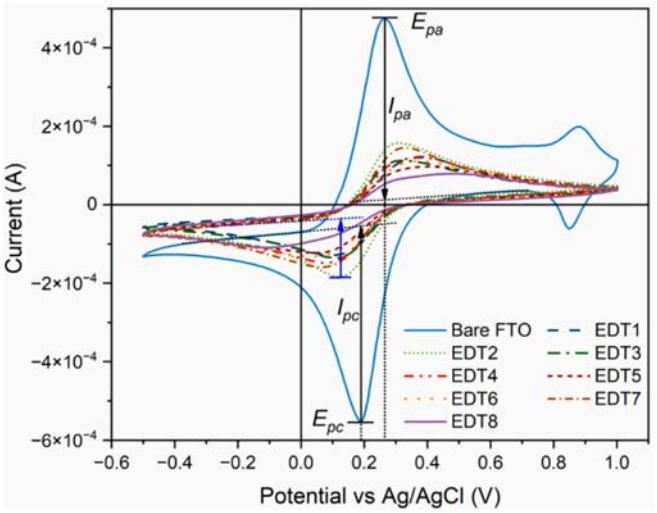

Fig. 9. Cyclic voltammetry (CV) curves for bare FTO and electrodeposited TiO_2 samples (EDT1-EDT8) in an electrolyte solution. The graph shows the current (A) as a function of the potential (V vs Ag/AgCl), indicating the redox behavior of the samples. The peaks correspond to the anodic (I_pa) and cathodic (I_pc) processes, with potential peaks at E_pa and E_pc, respectively. The red curve represents the bare FTO substrate, while other colors correspond to different TiO_2 samples. (For interpretation of the references to colour in this figure legend, the reader is referred to the web version of this article.)

underscores that a thicker TiO_2 layer enhances both light collection (*LHE*) and internal charge transport, leading to higher device efficiency [46].

To investigate the effect of duration and current densities for electrodeposited ETL on electron transfer in PSCs, the current density–voltage (*J-V*) characteristics of samples EDT1-EDT8 were compared with a control sample prepared using the spin-coated TiO_2 method as the ETL was analyzed. Fig. 13a shows the J-V characteristics of average-performing PSC devices, with corresponding parameters detailed in Table 2.

The PSCs utilizing EDT1-EDT8 exhibited reverse-scan *PCE* values of 8.14 %, 8.92 %, 9.12 %, 9.28 %, 6.36 %, 9.81 %, 10.83 %, and 9.66 %, respectively (Fig. 13a), significantly higher than the 6.85 % *PCE* for the spin-coated TiO_2 ETL sample. This improvement is due to an increase in both J_{SC} and V_{OC}. The J_{SC} increased from 18.1 mA cm^{-2} in the spin-coated sample to 18.46–20.06 mA cm^{-2} in EDT1-EDT8, while V_{OC} increased from 0.881 V in the spin-coated TiO_2 ETL sample to a range of 0.895 to 0.983 V in the EDT1-EDT8 samples. Additionally, except for EDT5, all electrodeposited TiO_2 samples show higher *FF* than the control. Furthermore, an increase in both current density and electrodeposition time for preparing the ETL correlates with an increase in *FF*. EDT6-EDT8, which had longer deposition durations, showed a noticeable increase in *FF*, with EDT7 exhibiting the highest *FF*. The Corresponding forward and reverse scans are shown in Figs. 13b and S4, with detailed PV performance parameters of PSCs fabricated by electrodeposited TiO_2 (EDT1-EDT8) and spin-coated TiO_2 (control) as the ETL are presented in Table 2. The higher V_{OC} and *FF* values were observed with electrodeposited ETL due to the successful fabrication of a pinhole-free TiO_2 thin film, which decreases electron recombination. This improvement facilitates better electron transport within the TiO_2 photoanode and lowers internal resistance. Table 2 shows that the hysteresis factor [7] for all samples is negligible, with EDT4 having the smallest factor. To better evaluate the quality of the prepared solar cells, the normalized parameters V_{OC}, J_{SC}, *FF*, *PCE*, series resistance (R_S), shunt resistance (R_{shunt}) and hysteresis factor (*HF*) were collected from *J-V* tests for PSCs using ETLs, including spin-coated TiO_2 as the control and EDT1-EDT8 (Fig. 13c). In this normalization, a value of 1 represents the highest quality, while a value of 0 represents the lowest. As indicated,

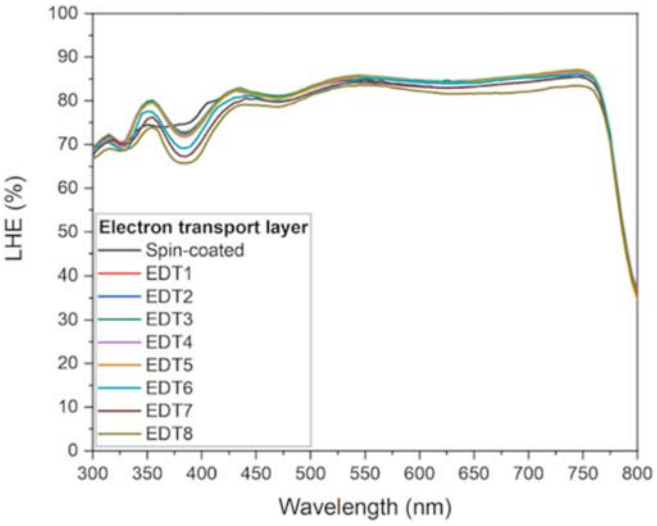

Fig. 11. LHE of the perovskite layer fabricated on the electrodeposited TiO_2-based working electrode for EDT1-EDT8 and spin-coated TiO_2 film.

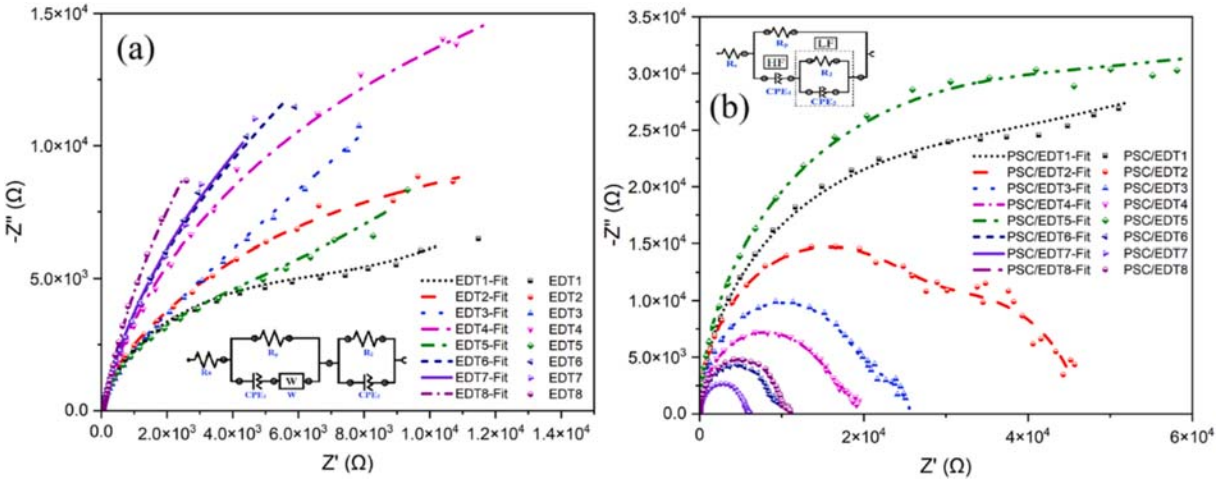

Fig. 10. Nyquist plots from Electrochemical Impedance Spectroscopy (EIS) for (a) EDT-modified samples and (b) PSC/EDT composites. Insets show the equivalent circuits used for fitting, with parameters including resistances (R), Warburg impedance (W), and constant phase elements (CPE).

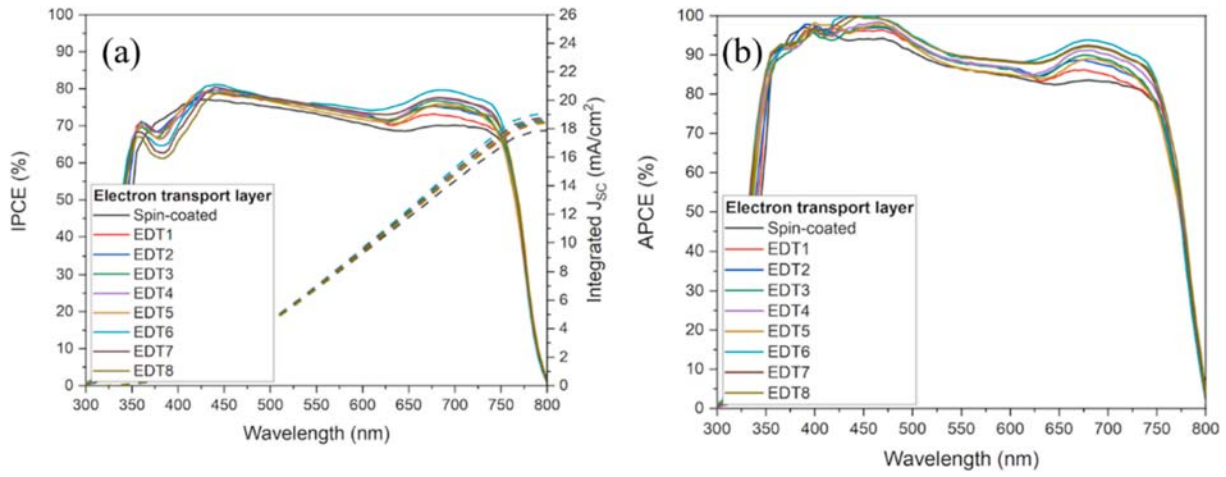

Fig. 12. (a) IPCE and (b) APCE spectra of the solar cells fabricated using the different electrodeposited ETL (EDT1-EDT8) and spin-coated TiO_2 film.

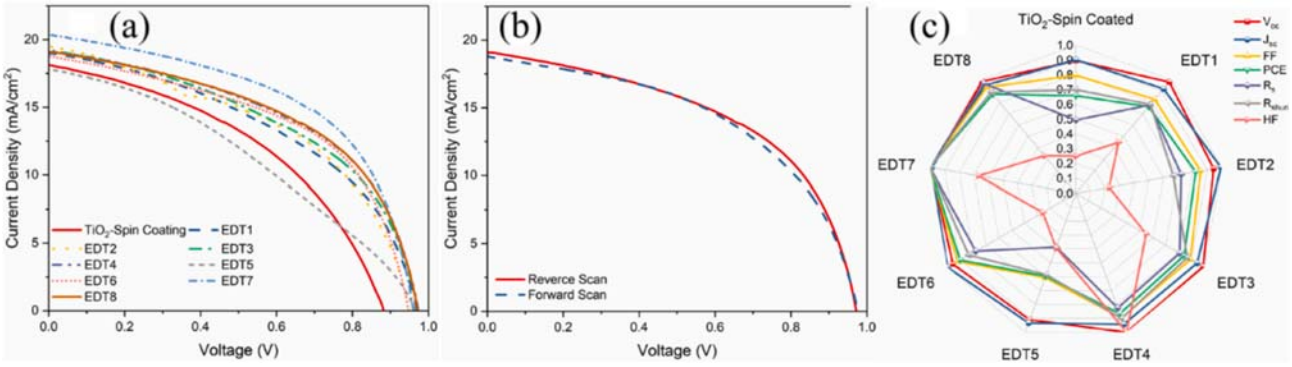

Fig. 13. PV performance analysis of EDT-modified solar cells. (a) J-V curves under standard illumination conditions for PV cells with different EDT treatments (EDT1 to EDT8) compared to a TiO_2 spin-coated reference. (b) J-V curves highlighting the hysteresis effect observed in forward and reverse scans. (c) Radar plot comparing key performance parameters, including V_{OC} , J_{SC} , FF, PCE, series resistance (R_s), shunt resistance (R_{shunt}), and hysteresis factor (HF) across the different samples.

the *PCE* with EDT7 as the ETL exhibits the best performance across nearly all parameters.

Stability testing is critical for assessing how well PSCs maintain efficiency over time under realistic conditions. To investigate device stability, samples were stored under ambient conditions with 45 % relative humidity, simulating aging in the dark. It's important to note that the test cells were not encapsulated, leaving the devices exposed to environmental degradation during testing. Fig. 14 shows the electrical measurements of PSCs fabricated with EDT1-EDT8, including the PV performance of ETL7 (inserted graph) after 168, 336 and 1000 h of aging. During the first 336 h, a 24 % to 29 % decrease in *PCE* was observed for all samples. After this, PSCs based on EDT6-EDT8 maintained stable efficiency for up to 1000 h. In contrast, the other samples showed a slight decline, with EDT5 exhibiting the most rapid decrease. These findings indicate that PSCs with thicker MLs and longer electrodeposition times have significantly higher stability compared to those with thinner MLs.

4. Conclusions

This study demonstrates the effectiveness of electrodeposition for developing high-performance ETLs for PSCs. By controlling current density and deposition duration, compact and mesoporous TiO_2 layers were optimized, significantly enhancing PV performance. Our findings indicate that adjusting the current density controls the compact layer quality, while both current density and electrodeposition time are key for optimizing ML morphology and performance. The PSCs fabricated using electrodeposited TiO_2 (EDT1-EDT8) improved the key PV parameters, such as J_{SC}, V_{OC} and *FF*, due to enhanced electron transport pathways and reduced recombination losses. The PSCs with thicker mesoporous layers (EDT6-EDT8) showed superior light collection and electron transport properties, achieving nearly perfect *APCE*. The optimized electrodeposited ETL (ETL7) exhibited a *PCE* improvement of up to 10.83 %, compared to 6.85 % achieved by the spin-coated TiO_2 used as a control ETL. The improved performance is attributed to better *LHE*, increased *IPCE*, and reduced charge recombination losses. Stability tests also revealed that PSCs with optimized ETLs maintained high efficiency for over 1000 h under ambient conditions. These findings underline the scalability and potential of electrodeposition for enhancing both efficiency and stability in carbon-based PSCs, offering a promising route for future commercial applications.

CRediT authorship contribution statement

Tecush Mohammadi: Writing – original draft, Investigation, Formal analysis, Conceptualization. **Dimitris A. Chalkias:** Formal analysis, Investigation, Characterization of the materials and devices, Writing – review & editing. **Nigel Van de Velde:** Investigation. **Andrej Race:** Investigation. **Elias Stathatos:** Writing – review & editing, Data curation. **Boštjan Genorio:** Investigation. **Blaž Likozar:** Funding acquisition. **Ivan Jerman:** Writing – review & editing, Funding acquisition, Data curation, Conceptualization.

Table 2
Summary of PV performance parameters for various samples, including TiO_2 spin-coated and EDT-treated cells.

		V_{oc} (V)	J_{sc} (mA cm^{-2})	FF %	PCE% (Average)	PCE% (Champion)	R_s (Ω)	R_{shunt} (Ω)	HF
TiO_2-Spin-coated	Forward Scan	0.879	17.15	43	6.42	6.42	236	2034	0.05162
	Reverse Scan	0.881	18.10	43	6.85	6.85	185	2346	
EDT1	Forward Scan	0.969	18.00	44	7.73 ± 0.30	8.03	123	2089	0.01001
	Reverse Scan	0.964	18.46	45	7.94 ± 0.40	8.14	118	2622	
EDT2	Forward Scan	0.935	20.18	46	8.25 ± 0.41	8.66	122	1524	0.00964
	Reverse Scan	0.928	19.94	46	8.54 ± 0.35	8.92	127	2238	
EDT3	Forward Scan	0.946	19.83	46	8.50 ± 0.10	8.57	139	1988	0.02470
	Reverse Scan	0.964	18.93	48	8.77 ± 0.26	9.12	113	2913	
EDT4	Forward Scan	0.992	18.68	48	8.75 ± 0.17	8.92	132	1686	0.02569
	Reverse Scan	0.983	18.92	48	9.02 ± 0.25	9.28	111	3021	
EDT5	Forward Scan	0.811	19.47	38	5.80 ± 0.15	5.94	259	1320	0.032942
	Reverse Scan	0.895	18.73	33	6.20 ± 0.10	6.36	236	1962	
EDT6	Forward Scan	1.025	18.04	51	9.10 ± 0.40	9.48	152	3130	0.04851
	Reverse Scan	0.942	20.06	50	9.38 ± 0.75	9.81	117	2800	
EDT7	Forward Scan	0.998	19.71	54	10.25 ± 0.35	10.59	110	2692	0.01368
	Reverse Scan	0.973	19.81	54	10.41 ± 0.40	10.83	91	3355	
EDT8	Forward Scan	0.975	18.87	49	8.55 ± 0.40	8.96	115	2483	0.12217
	Reverse Scan	0.969	19.09	50	9.08 ± 0.63	9.66	94	2984	

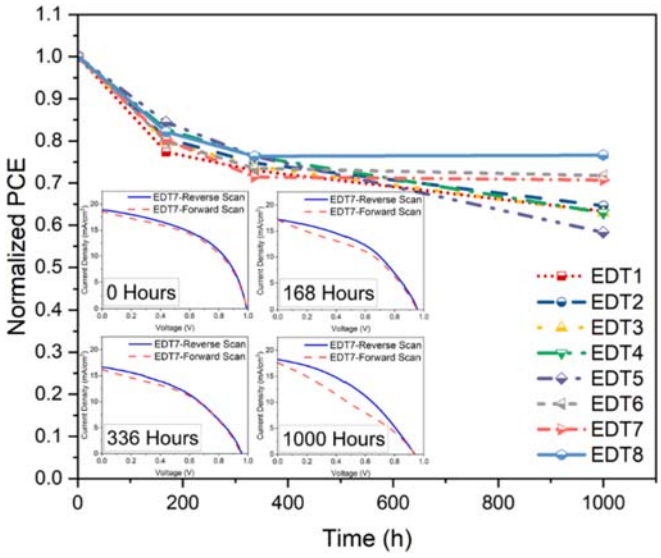

Fig. 14. Stability test showing normalized PCE over time for EDT-treated solar cells (EDT1 to EDT8) and PV results of sample with ETL7 (Inserted graphs).

Declaration of competing interest

The authors declare that they have no known competing financial interests or personal relationships that could have appeared to influence the work reported in this paper.

Acknowledgments

We would like to acknowledge the financial support by Slovenian Research and Innovation Agency research core funding No. P2-0393, as well as HyBReED project. Gratitude to Edi Kranjc for XRD measurements.

Appendix A. Supplementary data

Supplementary data to this article can be found online at https://doi.org/10.1016/j.solener.2025.113327.

References

[1] J.L. Holechek, H.M.E. Geli, M.N. Sawalhah, R. Valdez, A global assessment: can renewable energy replace fossil fuels by 2050? Sustainability 14 (2022) 4792.
[2] L.B. Kong, T. Li, H.H. Hng, F. Boey, T. Zhang, S. Li, in: Introduction, Waste Energy Harvesting: Mechanical and Thermal Energies, Springer Berlin Heidelberg, Berlin, Heidelberg, 2014, pp. 1–18.
[3] A.A. Bayod-Rújula, Solar photovoltaics (PV), in: Solar Hydrogen Production, Elsevier, 2019, pp. 237–295.
[4] B. Parida, S. Iniyan, R. Goic, A review of solar photovoltaic technologies, Renew. Sustain. Energy Rev. 15 (2011) 1625–1636.
[5] R.A. Afre, D. Pugliese, Perovskite solar cells: a review of the latest advances in materials, fabrication techniques, and stability enhancement strategies, Micromachines 15 (2024) 192.
[6] N.K. Elangovan, R. Kannadasan, B. Beenarani, M.H. Alsharif, M.-K. Kim, Z. H. Inamul, Recent developments in perovskite materials, fabrication techniques, band gap engineering, and the stability of perovskite solar cells, Energy Rep. 11 (2024) 1171–1190.
[7] A. Karavioti, B. Toplak, I. Jerman, E. Stathatos, Additive Engineering of Imidazolium-based cation for defect passivation with enhanced performance and stability of carbon-based perovskite solar cells, Mater. Sci. Semicond. Process. 171 (2024) 107992.
[8] S.R. Ali, M.M. Faisal, K. Sanal, M.W. Iqbal, Impact of carbon-based charge transporting layer on the performance of perovskite solar cells, Sol. Energy 221 (2021) 254–274.
[9] M. Bidikoudi, E. Stathatos, Carbon electrodes: the rising star for PSC commercialization, Electronics 12 (2023) 992.
[10] Z.W. Gao, Y. Wang, W.C. Choy, Buried interface modification in perovskite solar cells: a materials perspective, Adv. Energy Mater. 12 (2022) 2104030.
[11] S. Shao, M.A. Loi, The role of the interfaces in perovskite solar cells, Adv. Mater. Interfaces 7 (2020) 1901469.
[12] W.L. Lachore, D.M. Andoshe, M.A. Mekonnen, F.G. Hone, Recent progress in electron transport bilayer for efficient and low-cost perovskite solar cells: a review, J. Solid State Electrochem. 26 (2022) 295–311.

[13] Y. Pu, H. Su, C. Liu, M. Guo, L. Liu, H. Fu, A review on buried interface of perovskite solar cells, Energies 16 (2023) 5015.
[14] M. Dkhili, G. Lucarelli, F. De Rossi, B. Taheri, K. Hammedi, H. Ezzaouia, F. Brunetti, T.M. Brown, Attributes of high-performance electron transport layers for perovskite solar cells on flexible PET versus on glass, ACS Appl. Energy Mater. 5 (2022) 4096–4107.
[15] A.M. Elseman, C. Xu, Y. Yao, M. Elisabeth, L. Niu, L. Malavasi, Q.L. Song, Electron transport materials: evolution and case study for high-efficiency perovskite solar cells, Sol. RRL 4 (2020) 2000136.
[16] J. Lian, B. Lu, F. Niu, P. Zeng, X. Zhan, Electron-transport materials in perovskite solar cells, Small Methods 2 (2018) 1800082.
[17] N.E. Courtier, J.M. Cave, J.M. Foster, A.B. Walker, G. Richardson, How transport layer properties affect perovskite solar cell performance: insights from a coupled charge transport/ion migration model, Energ. Environ. Sci. 12 (2019) 396–409.
[18] J. Lee, J. Kim, C.-S. Kim, S. Jo, Compact SnO2/mesoporous TiO2 bilayer electron transport layer for perovskite solar cells fabricated at low process temperature, Nanomaterials 12 (2022) 718.
[19] R. Vanaraj, V. Murugesan, B. Rathinam, The role of optimal electron transfer layers for highly efficient perovskite solar cells—a systematic review, Micromachines 15 (2024) 859.
[20] J. Wang, X. Zhou, J. Ni, J. Guan, M. Hu, R. Wang, Y. Zhang, J. Li, H. Cai, J. Zhang, High-performance perovskite solar cell based on mesoporous TiO 2 electron transport layer enabled by composite treatment strategy, J. Mater. Sci. Mater. Electron. 32 (2021) 28417–28425.
[21] S.Y. Lin, T.S. Su, T.Y. Hsieh, P.C. Lo, T.C. Wei, Efficient plastic perovskite solar cell with a low-temperature processable electrodeposited TiO2 compact layer and a brookite TiO2 scaffold, Adv. Energy Mater. 7 (2017) 1700169.
[22] C. Zhen, T. Wu, R. Chen, L. Wang, G. Liu, H.-M. Cheng, Strategies for modifying TiO2 based electron transport layers to boost perovskite solar cells, ACS Sustain. Chem. Eng. 7 (2019) 4586–4618.
[23] T.-S. Su, T.-Y. Hsieh, C.-Y. Hong, T.-C. Wei, Electrodeposited ultrathin TiO2 blocking layers for efficient perovskite solar cells, Sci. Rep. 5 (2015) 16098.
[24] K.S. Anuratha, H.-S. Peng, Y. Xiao, T.-S. Su, T.-C. Wei, J.-Y. Lin, Electrodeposition of nanostructured TiO2 thin film as an efficient bifunctional layer for perovskite solar cells, Electrochim. Acta 295 (2019) 662–667.
[25] T.-S. Su, T.-C. Wei, Co-electrodeposition of Sn-doped TiO2 electron-transporting layer for perovskite solar cells, Physica Status Solidi (a), 217 (2020) 1900491.
[26] M.-S. Wu, C.-H. Tsai, T.-C. Wei, Anodic deposition of ultrathin TiO2 film with blocking layer and anchoring layer for dye-sensitized solar cells, J. Electrochem. Soc. 159 (2011) B80.
[27] T.S. Su, T.Y. Hsieh, T.C. Wei, Electrodeposited TiO2 film with mossy nanostructure for efficient compact layer in scaffold-type perovskite solar cell, Sol. RRL 2 (2018) 1700120.
[28] J. Robertson, Elements of X-ray Diffraction by BD Cullity, International Union of Crystallography, 1979.
[29] D. Chalkias, A. Karavioti, A. Kalarakis, E. Stathatos, Unveiling the importance of dripping temperature control of hybrid organic-inorganic perovskite precursor solution for the fabrication of fully ambient air-processed perovskite solar cells, Sol. Energy 224 (2021) 1017–1027.
[30] D. Chalkias, A. Karavioti, G. Papanicolaou, E. Stathatos, Stability assessment of carbon-based hole-transport-layer-free perovskite solar cells under accelerated ageing: a combined experimental and predictive modelling analysis, Electrochim. Acta 427 (2022) 140905.
[31] H. Fan, Z. Yang, X. Ren, M. Yin, F. Gao, S.F. Liu, Band alignment of TiO2/FTO interface determined by X-ray photoelectron spectroscopy: effect of annealing, AIP Adv. 6 (2016).
[32] S. Benkoula, O. Sublemontier, M. Patanen, C. Nicolas, F. Sirotti, A. Naitabdi, F. Gaie-Levrel, E. Antonsson, D. Aureau, F.-X. Ouf, Water adsorption on TiO2 surfaces probed by soft X-ray spectroscopies: bulk materials vs. isolated nanoparticles, Sci. Rep. 5 (2015) 15088.
[33] R. Sivakumar, J. Ramkumar, S. Shaji, M. Paulraj, Efficient TiO2 blocking layer for TiO2 nanorod arrays-based dye-sensitized solar cells, Thin Solid Films 615 (2016) 171–176.
[34] S. Sen, J. Riga, J. Verbist, 2s and 2p X-ray photoelectron spectra of Ti4+ ion in TiO2, Chem. Phys. Lett. 39 (1976) 560–564.
[35] A. Sławek, Z. Starowicz, M. Lipiński, The influence of the thickness of compact TiO2 electron transport layer on the performance of planar CH3NH3PbI3 perovskite solar cells, Materials 14 (2021) 3295.
[36] W. Wang, Z. Zhang, Y. Cai, J. Chen, J. Wang, R. Huang, X. Lu, X. Gao, L. Shui, S. Wu, Enhanced performance of $CH_3NH_3PbI_{3-x}Cl_x$ perovskite solar cells by CH_3NH_3I modification of TiO_2-perovskite layer interface, Nanoscale Res. Lett. 11 (2016) 1–9.
[37] R.K. Poobalan, R. Ramanathan, R. Chellakumar, K. Ravichandran, M. Zinigrad, Enhancing the perovskite solar cell performance by the interface modification of Zn–Sn–O compound heterostructures, Mater. Adv. 4 (2023) 6704–6717.
[38] Y. Wang, W. Fu, J. Yan, J. Chen, W. Yang, H. Chen, Low-bandgap mixed tin–lead iodide perovskite with large grains for high performance solar cells, J. Mater. Chem. A 6 (2018) 13090–13095.
[39] E. Von Hauff, D. Klotz, Impedance spectroscopy for perovskite solar cells: characterisation, analysis, and diagnosis, J. Mater. Chem. C 10 (2022) 742–761.
[40] M. Taukeer Khan, A. Almohammedi, S. Kazim, S. Ahmad, Electrical methods to elucidate charge transport in hybrid perovskites thin films and devices, Chem. Rec. 20 (2020) 452–465.
[41] I. Zarazua, S. Sidhik, T. Lopez-Luke, D. Esparza, E. De la Rosa, J. Reyes-Gomez, I. Mora-Sero, G. Garcia-Belmonte, Operating mechanisms of mesoscopic perovskite solar cells through impedance spectroscopy and J–V modeling, J. Phys. Chem. Lett. 8 (2017) 6073–6079.
[42] I. Zarazua, G. Han, P.P. Boix, S. Mhaisalkar, F. Fabregat-Santiago, I. Mora-Seró, J. Bisquert, G. Garcia-Belmonte, Surface recombination and collection efficiency in perovskite solar cells from impedance analysis, J. Phys. Chem. Lett. 7 (2016) 5105–5113.
[43] D.A. Chalkias, A. Nikolakopoulou, L.C. Kontaxis, A.N. Kalarakis, E. Stathatos, Record-breaking efficient and mechanically-robust ambient-air-processed carbon-based flexible perovskite photovoltaics through effective and benign-to-plastics green-antisolvent quenching, Adv. Funct. Mater. (2024) 2406354.
[44] A.D. Sheikh, A. Bera, M.A. Haque, R.B. Rakhi, S. Del Gobbo, H.N. Alshareef, T. Wu, Atmospheric effects on the photovoltaic performance of hybrid perovskite solar cells, Sol. Energy Mater. Sol. Cells 137 (2015) 6–14.
[45] J. Huang, S. Xiang, J. Yu, C.-Z. Li, Highly efficient prismatic perovskite solar cells, Energ. Environ. Sci. 12 (2019) 929–937.
[46] D.A. Chalkias, A. Mourtzikou, G. Katsagounos, A. Karavioti, A.N. Kalarakis, E. Stathatos, Suppression of coffee-ring effect in air-processed inkjet-printed perovskite layer toward the fabrication of efficient large-sized all-printed photovoltaics: a perovskite precursor ink concentration regulation strategy, Sol. RRL 6 (2022) 2200196.